water

MDPI

Article

Optical Ring and Integral AUC Analysis for Determining the Apparent Contact Angle of Sessile Water Drops with FT-IR and XPS Analyses

Ignat Ignatov [1,2,*], Yordan G. Marinov [2,*], Alexander I. Ignatov [1], Paunka Vassileva [3] and Georgi Gluhchev [4]

[1] Scientific Research Center of Medical Biophysics (SRCMB), 1111 Sofia, Bulgaria
[2] Georgi Nadjakov Institute of Solid State Physics, Bulgarian Academy of Sciences, 72 Tzarigradsko Chaussee Blvd., 1784 Sofia, Bulgaria
[3] Institute of General and Inorganic Chemistry, Bulgarian Academy of Sciences, 1113 Sofia, Bulgaria; pnovachka@svr.igic.bas.bg
[4] Institute of Information and Communication Technologies, Bulgarian Academy of Sciences, 1113 Sofia, Bulgaria
* Correspondence: mbioph@abv.bg (I.I.); ymarinov@issp.bas.bg (Y.G.M.); Tel.: +359-895-533-779 (I.I.)

Abstract

A previous study by the authors established and experimentally validated a geometrical–optical method for determining the apparent contact angle of sessile water drops from the dark optical ring formed in a water–Mylar–glass system. The present work extends this approach to a practical comparison between two BoPET surfaces with different surface states: untreated Mylar 1 and factory corona-treated Mylar 2. Distilled water from the same batch was used on both surfaces, and the apparent contact angle was monitored at 5 min intervals throughout complete evaporation. The time-dependent contact-angle curves were evaluated by full-process area-under-the-curve (AUC) analysis and by a dimensionless apparent wettability parameter, $H(t) = [1 + \cos(\theta)]/2$, calculated from the contact angles. For Mylar 1, complete evaporation lasted 270 min and yielded an AUC of 11,023.06 ± 60.06 °·min, whereas for Mylar 2, the corresponding values were 245 min and 9322.70 ± 20.1 °·min. The initial apparent contact angle decreased from 67.2° for Mylar 1 to 61.1° for Mylar 2, while the normalized wettability parameter increased from 0.694 to 0.742. The reported XPS O/C atomic ratios were approximately 0.32 for Mylar 1 and 0.47 for Mylar 2, suggesting a higher relative surface oxygen content in Mylar 2. The results demonstrate the applicability of contact-angle monitoring combined with AUC analysis over the common observation interval for distinguishing the evaporation-driven apparent wetting behavior of untreated and corona-treated BoPET surfaces.

Keywords: sessile drop; apparent contact angle; optical ring method; hydrophilic; AUC analysis; evaporation dynamics; interfacial relaxation; Mylar; FT-IR; XPS

Check for updates

Academic Editor: Zhijun Li

Received: 27 September 2026
Revised: 23 October 2026
Accepted: 27 October 2026
Published: 28 October 2026

Copyright: © 2026 by the authors. Licensee MDPI, Basel, Switzerland. This article is an open access article distributed under the terms and conditions of the Creative Commons Attribution (CC BY) license.

1. Introduction

Wetting is a fundamental interfacial phenomenon in soft matter, colloid science, materials science, and biological systems. The contact angle [1,2] of a liquid drop [1,3] on a solid surface [1,2] represents a macroscopic manifestation of the balance between solid–vapor, solid–liquid, and liquid–vapor interfacial interactions [1,4]. For this reason, it is widely used as a quantitative descriptor of hydrophilicity and hydrophobicity [1,4], adhesion [2,5], surface energy [2], and dynamic wetting behavior [6,7]. In the case of water, the contact angle is of particular interest because the macroscopic geometry of a sessile drop is coupled

not only to surface tension and substrate properties, but also to evaporation, contact-line motion, and the internal organization of the hydrogen-bonded liquid structure [8,9].

The evaporation of a sessile water drop is a dynamic process in which the apparent contact angle, contact radius, drop height, and drop volume evolve simultaneously. Depending on the liquid–solid system and environmental conditions, evaporation may proceed through different modes, including constant-contact-radius, constant-contact-angle, mixed-mode, and stick–slip contact-line motion [10–13]. These modes are controlled by contact-line pinning, surface heterogeneity, substrate wettability, vapor diffusion, and capillary flow within the sessile drop [10–12]. Therefore, time-resolved contact-angle measurements provide more information than a single static contact-angle value: they describe the temporal evolution of the sessile-drop geometry and the stability of the liquid–solid–air interface during evaporation.

Classical optical and goniometric methods determine the contact angle by analyzing the profile of a sessile drop. Such approaches are well established; accurate contact-angle determination can become challenging under demanding measurement conditions, particularly at very low contact angles and during dynamic measurements, while goniometric accuracy may also be affected by drop dimensions, image analysis, baseline determination, and profile fitting [14]. Optical microscopy-based techniques have, therefore, been developed for dynamic measurements at low contact angles [15]. Other authors have used evaporation itself as a tool for determining dynamic and receding contact angles. In this context, previous studies have investigated the evaporation of microdroplets as a probe for wetting on solid surfaces [16] and demonstrated that the receding contact angle on polymer surfaces can be determined from the time-dependent evaporation of sessile drops [17]. These studies established that evaporation-driven contact-angle evolution is not merely an experimental complication, but also a valuable source of information about wetting dynamics.

A major contribution to this field is the recognition that the apparent contact angle during evaporation reflects both interfacial geometry and contact-line dynamics. Bourges-Monnier and Shanahan showed that evaporation can significantly influence the measured contact angle [10]. Hu and Larson analyzed the evaporation of sessile droplets and demonstrated the importance of internal flow and vapor diffusion in determining drop evolution [11]. More recent theoretical and experimental studies have further clarified the roles of substrate hydrophobicity, pinning–depinning transitions, and stick–slip behavior during evaporation [12,18,19]. Thus, modern contact-angle analysis increasingly requires not only a geometrical measurement but also a time-resolved interpretation of the drop as an evolving interfacial system.

Recent studies have further expanded the experimental and theoretical understanding of contact-angle evolution during sessile-drop evaporation. Starinskaya et al. investigated the evaporation dynamics of sessile and suspended almost-spherical water drops on biphilic surfaces and showed that drop orientation, surface design, and thermal conditions can significantly modify evaporation pathways [20]. Tian et al. applied molecular kinetic theory to investigate the roles of liquid viscosity and solid-surface properties in the dynamic wetting of solid–liquid–liquid systems [21]. Their study provides complementary theoretical context, although direct application to the present evaporating water–Mylar–air system would require separate validation. Srinivasan et al. examined the accuracy of contact-angle measurements for sessile drops on liquid-repellent surfaces, highlighting the importance of measurement accuracy when characterizing wetting behavior [22]. Antonov et al. developed simple and advanced models for the heating and evaporation of sessile droplets, emphasizing the need to combine experimental contact-angle data with physically grounded evaporation models [23]. Kavuri et al. recently investigated isolated and

paired sessile water drops on heated superhydrophobic substrates, showing that vapor shielding, substrate temperature, and constant-contact-angle or mixed evaporation modes strongly affect drop lifetime and contact-angle evolution [8]. Together, these recent studies confirm that the contact angle of an evaporating sessile drop is a dynamic quantity influenced by surface wettability, contact-line mobility, thermal transport, vapor diffusion, and evaporation mode.

In this context, the geometrical–optical method provides an additional non-invasive approach for determining the apparent contact angle of sessile water drops [9]. The method is based on the passage of light through a multilayer optical system consisting of water, Mylar, and glass. By applying Snell's law and the principles of geometrical optics, the radius of the dark optical ring formed by refraction is related to the apparent contact angle of the evaporating sessile water drop. This approach differs from conventional profile-based goniometry because it does not rely primarily on direct visualization of the drop contour. Instead, it uses the optical-ring geometry as an indirect but quantitative indicator of the sessile water drop shape and its time-dependent evolution.

An important advantage of the optical-ring method is that it allows the apparent contact angle to be monitored repeatedly during evaporation under standardized experimental conditions. This makes it possible to follow the entire relaxation pathway of the sessile water drop, from the initial wetting state to the final stage of evaporation. When the contact-angle values are integrated over time, the area under the curve (AUC) provides a quantitative measure of the cumulative preservation of sessile water drop geometry. A higher AUC value indicates that the sessile water drop preserves larger apparent contact angles over a longer evaporation interval, whereas a lower AUC value reflects faster contact-angle relaxation, enhanced spreading, or more rapid loss of sessile-drop geometry during evaporation.

For water systems, this time-integrated optical parameter is of particular interest because water is a hydrogen-bonded liquid. Changes in evaporation dynamics may be consistent with differences in interfacial organization and hydrogen-bond-related relaxation behavior. However, contact-angle and AUC measurements are macroscopic, indirect indicators. They do not directly resolve hydrogen bonds at the molecular level and should not be used alone to quantify hydrogen-bond number, energy, or lifetime. Their scientific value becomes stronger when they are combined with complementary techniques, such as NMR, FT-IR spectroscopy, electrical impedance spectroscopy (EIS), and quantum-chemical modeling of small water clusters [9]. In such a multiscale framework, contact-angle evolution can be discussed in relation to interfacial wetting behavior, evaporation kinetics, and possible differences in the broader structural organization of water.

The approach is particularly useful for distinguishing water samples that may show only small differences in the initial contact-angle measurements but exhibit pronounced differences during the full evaporation process. In this way, the AUC method extends classical contact-angle analysis from a static measurement to a dynamic, time-integrated descriptor of the water–surface interaction.

Thus, the present work builds upon classical wetting theory, evaporation studies of sessile droplets, dynamic optical contact-angle methods, and the geometrical–optical approach. Its main contribution is the use of optical-ring measurements and AUC analysis as a time-integrated approach for evaluating the evaporation-driven evolution of sessile water drops and surface hydrophilicity. This approach provides a physically meaningful link between macroscopic wetting behavior and potential differences in interfacial organization during evaporation.

2. Materials and Methods

2.1. Water Drop–Mylar–Glass System

The method is based on the observation of a dark optical ring formed by light refraction in the water drop–Mylar–glass system. The geometry of this ring is related to the apparent contact angle of the sessile drop [9]. The optical–geometrical basis of this approach has been previously demonstrated [9]. Figure 1 illustrates the experimentally validated setup for determining the apparent contact angle of a sessile water drop through refraction in a multilayer system consisting of water, Mylar film, and glass. The measured optical-ring parameter (a) is related to the apparent contact angle (θ) by applying Snell's law at the water–film and film–glass interfaces.

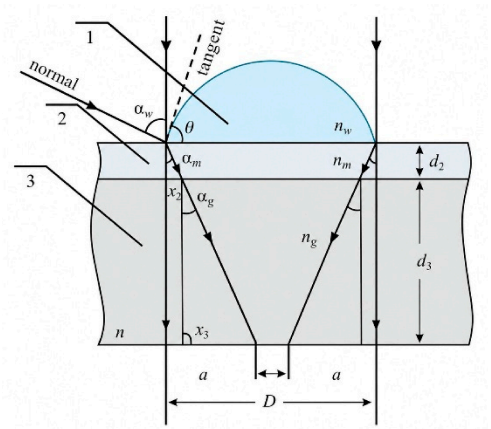


Figure 1. Experimentally validated optical–geometrical scheme for determining the apparent contact angle of a sessile water drop from the optical-ring displacement in the water–Mylar–glass system, based on the method reported in [9].

The geometrical–optical relationship is expressed as follows [9]:

$$a(\theta) = d_2 \tan\left[\arcsin\left(\frac{n_w \sin\theta}{n_m}\right)\right] + d_3 \tan\left[\arcsin\left(\frac{n_w \sin\theta}{n_g}\right)\right]$$

For $d_2 \ll d_3$, the apparent contact angle is calculated using the expression [9]:

$$\theta(a) \approx \arcsin\left(\frac{n_g}{n_w}\right)\left(\frac{\frac{a}{d_3}}{\left(1+\left(\frac{a}{d_3}\right)^2\right)^{\frac{1}{2}}}\right)$$

This provides an independent geometrical–optical method for evaluating the contact angle without direct fitting of the sessile drop profile, thereby supporting the reliability of the optical-ring approach used for analyzing sessile water drops.

The parameters of the geometry are as follows: θ is the apparent contact angle; d_2 is the Mylar thickness, 12 ± 1 μm; d_3 is the glass thickness, 1.00 ± 0.05 mm; the refractive index of water is $n_w = 1.333 \pm 0.002$; the refractive index of Mylar is $n_m = 1.58 \pm 0.01$; and the refractive index of glass is $n_g = 1.50 \pm 0.01$ [9].

For each time point, a characteristic linear parameter of the optical ring is measured. Then, using the geometrical–optical relationship reported in [9], this parameter is converted into a value of the apparent contact angle. In this way, instead of directly measuring the drop profile, the optical image of the sessile drop is analyzed, making the method applicable for monitoring drop dynamics during evaporation.

2.2. Parameters of the Mylar Surfaces

Two biaxially oriented polyethylene terephthalate (BoPET, Mylar) films with different surface states were investigated: an untreated Mylar surface (Mylar 1) [MYLAR® LB 48, Mylar Speciality Films (formerly DuPont Tejin Films), Redcar, UK] and a factory corona-treated Mylar surface (Mylar 2) (MYLAR® LB 48 Specialty Films). Corona treatment is an established industrial surface-modification procedure for BOPET films and is commonly applied during film manufacture to increase surface polarity, surface free energy, wettability, and adhesion [24–26]. In the present study, corona treatment of Mylar 2 was performed industrially prior to delivery; no additional corona, plasma, chemical, or mechanical surface treatment was applied by the authors, and both films were used as received.

The Mylar films had a thickness of 12 ± 1 µm (nominal thickness 12 µm for both commercial grades) and were supported on identical glass substrates with a thickness of 1.00 ± 0.05 mm. The corona-treated side of Mylar 2 was oriented toward the sessile water drop during all measurements. Distilled water from the same batch was used as the probe liquid for both surfaces. An identical drop volume, optical configuration, measurement interval, temperature, and relative humidity were maintained for both substrates, allowing differences in apparent contact-angle behavior to be evaluated primarily as differences in the wetting properties of the two Mylar surface states.

Previous surface-characterization studies of BOPET have demonstrated that corona treatment increases surface energy and wettability and modifies the surface chemistry and morphology of the polymer [24–26]. Barbaro et al. investigated commercial untreated and corona-treated BOPET films, with the corona treatment performed in-line during film production, and reported increased surface energy and improved interfacial adhesion after treatment [24]. Ding et al., using ATR-FTIR, XPS, SEM, and AFM, demonstrated the formation of polar surface functionalities and surface modification of BOPET following corona discharge treatment [25].

Contact-angle and XPS studies of corona-treated PET have likewise demonstrated pronounced changes in surface oxidation and wettability [26]. According to the manufacturer's technical specification, MYLAR® LBT is an uncoated transparent polyester film supplied with one-side corona treatment and commercially available at a nominal thickness of 0.48 mil (12 µm). The corresponding MYLAR® LB film is available without corona treatment, whereas MYLAR® LBT2 is corona-treated on both sides [27]. These specifications correspond to the untreated and factory corona-treated grades investigated in the present study.

2.3. Fourier Transform Infrared (FT-IR) Spectroscopy

The Mylar samples were analyzed using Fourier-transform infrared (FT-IR) spectrometry. The FT-IR spectra were recorded using a Thermo Nicolet Avatar 360 FT-IR spectrometer (Waltham, MA, USA), equipped with a DTGS detector, over the spectral range of 400–4000 cm^{-1}, with 64 scans accumulated at a spectral resolution of 2 cm^{-1} [28–30]. The experiments were performed at 298.15 K. The FT-IR spectra of Mylar 1 and Mylar 2 were recorded in transmission mode. All measurements were conducted at the Institute of General and Inorganic Chemistry, Bulgarian Academy of Sciences (BAS), Sofia, Bulgaria.

2.4. X-Ray Photoelectron Spectroscopy (XPS)

X-ray photoelectron spectroscopy (XPS) was used to characterize the surface chemical composition of untreated Mylar 1 and factory corona-treated Mylar 2. Survey spectra were used to determine the relative atomic concentrations of carbon and oxygen based on the C 1s and O 1s signals, and the O/C atomic ratio was calculated as an indicator of surface oxidation. High-resolution C 1s spectra were additionally analyzed to evaluate

the relative contributions of C–C/C–H, C–O, and O–C=O chemical environments. The measurements were performed on the surface exposed to the sessile water drop in the contact-angle experiments.

A Leybold LHS-10 electron spectrometer (Leybold, Cologne, Germany), equipped with an Al Kα X-ray source (1486.6 eV), was used for the measurements. The X-ray source was positioned at 45° to the sample surface, while the hemispherical electrostatic electron-energy analyzer was oriented normal to the surface. The analysis vacuum was approximately 5×10^{-8} mbar [31].

2.5. Data Processing

The contact angle is expressed as a function of time: $\theta = f(t)$.

The zonal decrease rate of the apparent contact angle is defined as:

$$k_\theta = (\theta_{start} - \theta_{end})/(t_{end} - t_{start})$$

and is expressed in $^\circ \cdot min^{-1}$.

For comparison between the curves, the following is used:

$$AUC = \int_{t_0}^{T} \theta(t)dt \quad (1)$$

where AUC is the area under the curve, t_0 is the initial measurement time, and T is the final measurable time of the complete evaporation process for each individual sessile water drop.

For the point-by-point comparison of Mylar 1 (control) and Mylar 2 (sample) over their common time interval, the following quantity was used:

$$\Delta\theta(t) = \theta_{sample\,(t)} - \theta_{control\,(t)} \quad (2)$$

This quantity represents the instantaneous difference in the apparent contact angle between Mylar 1 and Mylar 2 at corresponding time points. For positive values of $\Delta\theta(t)$, the sample exhibits a higher apparent contact angle than the control, and for larger values, the effect is more pronounced.

For the quantitative evaluation of the overall effect of the sample relative to the control, the time integral of this difference was also calculated:

$$\Delta AUC = \int_{t_0}^{T} \Delta\theta(t)dt = \int_{t_0}^{T} \left[\theta_{sample}(t) - \theta_{control}(t)\right]dt \quad (3)$$

Equation (3) is applicable only over a time interval in which both contact-angle curves are defined and referred to the same time origin. If the observation intervals differ, the integral must be restricted to their common interval; it must not be calculated by subtracting full-process AUC values obtained over different durations. When the curves cross, positive and negative differences may cancel out, so the resulting integral describes the net difference rather than the total magnitude of their separation. In the processing of the discrete experimental data, the integral quantities AUC and $\int\Delta\theta(t)dt$ were calculated numerically using the trapezoidal rule.

The use of an area-under-the-curve approach is well established for the quantitative evaluation of time-dependent experimental responses. By analogy, in the present study, the apparent contact angle, $\theta(t)$, is treated as a time-dependent experimental function, and the integral AUC represents the cumulative preservation of the apparent contact angle during evaporation. Thus, the AUC parameter provides a time-integrated descriptor over the complete evaporation process. For each surface, the AUC was calculated from t_0 to T; consequently, the integral incorporates both the magnitude $\theta(t)$ and the duration of the complete evaporation process.

2.6. Goniometrical Measurement of Contact Angle and Parameters of Water Drops

Contact-angle and sessile drop-geometry measurements were obtained using the Easy Drop shape analysis system DSA20E (KRÜSS GmbH, Hamburg, Germany) and KRÜSS Drop Shape Analysis DSA1 software (version V1.92-05) [9]. Distilled water was used for instrumental validation and calibration of the goniometric setup. The comparative evaporation experiments reported in the present study were performed with Mylar 1 and Mylar 2.

For the optical-ring evaporation measurements, 20 µL drops were used to ensure clear visualization of the dark refractive ring.

All evaporation experiments were carried out under ambient laboratory conditions at the temperature [25 ± 0.5] °C and a relative humidity of [51 ± 2] % [9].

3. Results

3.1. FT-IR Analysis of the Surface Chemical Composition of Untreated Mylar 1 and Corona-Treated Mylar 2

Figure 2 presents the FT-IR spectra of untreated Mylar 1 (a,b) and factory corona-treated Mylar 2 (c,d). ATR-FTIR spectroscopy has previously been applied to untreated and corona-treated BOPET films to evaluate treatment-induced changes in the polymer surface and its characteristic functional groups [24,25].

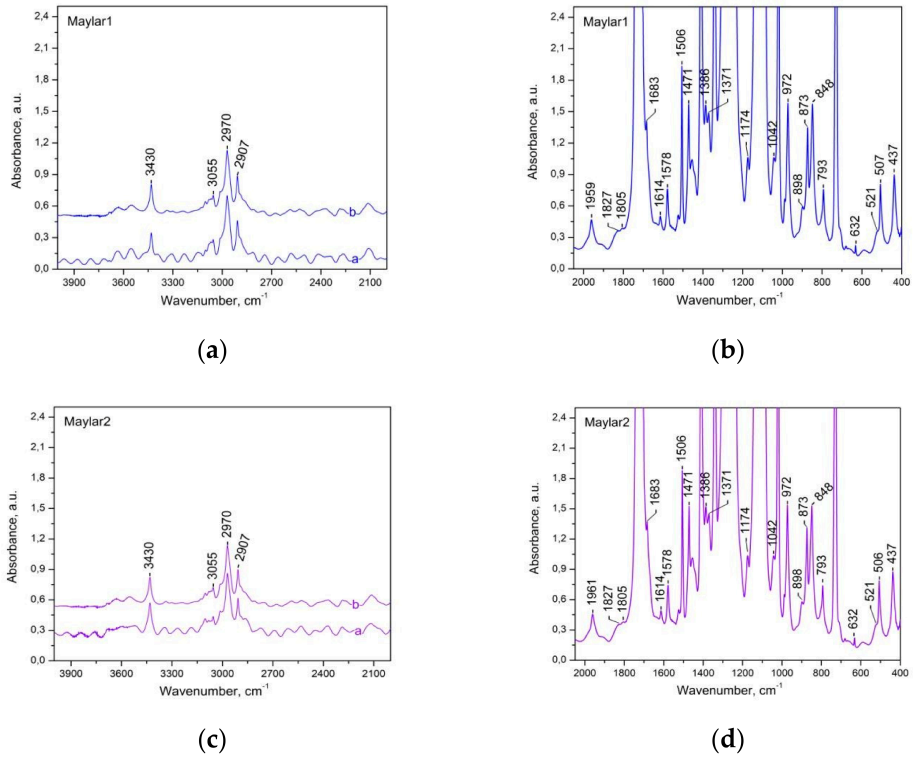


Figure 2. FT-IR spectra of untreated Mylar 1 (**a**,**b**) and factory corona-treated Mylar 2 (**c**,**d**).

The FT-IR spectra of Mylar 1 and Mylar 2 retain the characteristic absorption pattern of BoPET, and no pronounced shifts or newly resolved absorption bands are observed under the present experimental conditions. Thus, the factory corona treatment did not produce changes that could be clearly distinguished from the dominant PET vibrational bands by the applied FT-IR analysis. This observation does not exclude chemical modification of the outermost polymer layer, because corona treatment of BOPET/PET is known to induce surface oxidation and the formation of oxygen-containing polar functionalities [24–26].

Such near-surface chemical changes are more directly characterized by XPS, which probes the outermost region of polymer surfaces and is particularly suitable for detecting treatment-induced changes in elemental composition and chemical bonding [25,26,32].

3.2. XPS Analysis of the Surface Chemical Composition of Untreated Mylar 1 and Factory Corona-Treated Mylar 2

Previous studies by Ignatov and co-authors have investigated the ionization processes and physicochemical changes associated with corona gas discharge in aqueous systems [33–35]. Corona discharge is accompanied by gas-phase ionization and the formation of reactive oxygen- and nitrogen-containing species, while experiments with aqueous $CaCO_3$ solutions have shown changes in electrical conductivity, pH, and OH^- concentration after corona-discharge exposure [34,35]. In the present study, XPS provides direct information on the surface chemical composition of the solid polymer and allows the effects of corona treatment on the Mylar surface to be evaluated.

XPS analysis revealed clear differences in the surface chemical composition of untreated Mylar 1 and corona-treated Mylar 2 (Table 1). The corona-treated surface showed a lower relative carbon content and a higher oxygen content. Based on the measured atomic concentrations of approximately 76 at.% C and 24 at.% O for Mylar 1 and 68 at.% C and 32 at.% O for Mylar 2, the corresponding O/C atomic ratios were approximately 0.32 and 0.47, respectively. The available C 1s analysis suggests a relative decrease in the non-polar C–C/C–H contribution and an increased contribution of oxygen-containing C–O and O–C=O functionalities in Mylar 2. However, these oxygen-containing groups are also inherent to the PET structure, particularly its ester groups. These changes are compatible with possible differences in surface oxidation between the two films. The increased surface polarity may provide a surface-chemical explanation for the lower water contact angle and increased wettability observed for Mylar 2.

Table 1. XPS surface chemical composition and qualitative C 1s component comparison of untreated Mylar 1 and factory corona-treated Mylar 2.

XPS Parameters	Mylar 1, Untreated	Mylar 2, Corona-Treated	Interpretation
C 1s, at. %	~76	~68	decrease in relative carbon contribution
O 1s, at. %	~24	~32	increase in surface oxygen
O/C, atomic ratio	~0.32	~0.47	increased surface oxidation

3.3. AUC Analysis

The XPS results are interpreted qualitatively, taking into account the intrinsic ester groups of PET and the limitations of the available surface-composition data.

3.4. AUC Analysis of Distilled Water on Mylar 1 and Mylar 2

Distilled water was used on both Mylar surfaces; the comparison reflects the different wetting and evaporation behavior of untreated Mylar 1 and factory corona-treated Mylar 2. The results show a gradual decrease in the apparent contact angle over time, reflecting the natural evaporation process and the accompanying change in drop geometry.

For the distilled water on Mylar 1, the full measurement interval included 55 time points, corresponding to 0–270 min, and the calculated AUC was 11,023.06 ± 60.06 °·min. For the distilled water on Mylar 2, the full measurement interval included 50 time points, corresponding to 0–245 min, and the calculated AUC was 9322.75 ± 26.10 °·min. Thus, the full-curve AUC for Mylar 1 was higher by 1700.75 °·min, corresponding to +18.24% relative to Mylar 2. For statistical comparison over the common interval of 0–245 min, the

AUC was higher for Mylar 1 than for Mylar 2 (10,570.81 ± 62.10 vs. 9322.70 ± 26.10 °·min; mean ± SD; n = 5 drops per group). The mean difference was 1248.11 °·min (95% CI: 1178.64–1317.58 °·min; two-tailed Student's *t*-test assuming equal variances: t(8) = 41.432, $p = 1.27 \times 10^{-10}$).

To account for the different measurement durations, AUC was normalized by time (AUC/T), yielding mean apparent contact angles of 40.8° for Mylar 1 and 38.1° for Mylar 2.

AUC is an established integral summary measure for repeated time-dependent observations [36,37]. The higher measured-interval AUC for Mylar 1 reflects the combined contribution of larger apparent contact-angle values and a longer measurable evaporation interval (270 versus 245 min). Because the purpose of the integral analysis is to characterize the entire evaporation process, the different endpoint times are part of the measured response and are included in the AUC.

The endpoints of 270 min (Mylar 1) and 245 min (Mylar 2) represent the last measurable contact-angle values rather than the exact times of complete sessile drop disappearance. Measurements were performed at 5 min intervals, and AUC was calculated by the trapezoidal rule using only measured values without extrapolation beyond the final measurement.

The AUC values are presented as mean ± standard deviation (SD) for five independent sessile water drops per group (n = 5). Student's two-tailed *t*-test revealed a statistically significant difference between Mylar 1 and Mylar 2 (t = 41.432, df = 8, $p = 1.27 = \times 10^{-10}$) (Figure 3). These results indicate a statistically significant difference in the full-process time-integrated apparent contact-angle behavior of distilled water on Mylar 1 and Mylar 2.

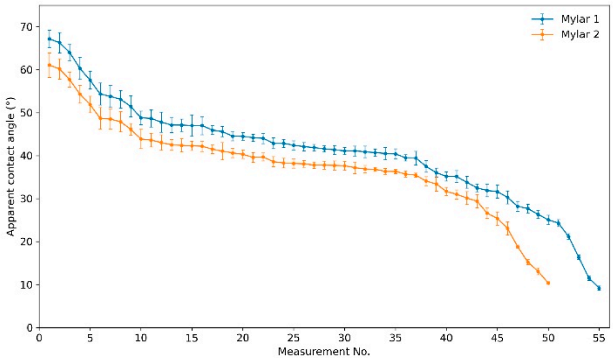


Figure 3. Distilled water on Mylar 1 maintained higher apparent contact angles over time than Mylar 2 during the evaporation process.

The observed dependence θ = f(t) for both samples shows a generally decreasing trend during evaporation. However, distilled water on Mylar 1 maintained higher apparent contact angle values and exhibited a longer complete evaporation time than distilled water on Mylar 2.

The contact angle is given as a function of time:

$$\theta = f(t) \tag{4}$$

Since the measurements are performed at equal time intervals, the integral can be approximated as:

$$AUC \approx \sum_{i=1}^{n-1} \frac{\theta_i + \theta_{i+1}}{2} \Delta t \tag{5}$$

where θ_i and θ_{i+1} are consecutive measured values of the contact angle; Δt is the constant time interval between measurements (5 min).

3.5. Normalized Wettability Parameter and Full-Process Integral Hydrophilicity Analysis

To express the time-dependent wetting behavior in dimensionless form, a dimensionless normalized wettability parameter, H(t), was additionally defined from the apparent contact angle using a normalized Young–Dupré-type relationship:

$$H(t) = \frac{1 + cos\ \theta(t)}{2} \tag{6}$$

where θ(t) is the apparent contact angle at time t. The parameter is dimensionless and increases as the apparent contact angle decreases. Thus, larger H(t) values correspond to greater hydrophilicity and wettability of the investigated surface.

The cumulative hydrophilic response over the observation interval was then quantified as the area under the hydrophilicity curve:

$$AUC_H = \int_0^T H(t)dt \tag{7}$$

Here, H(t) is dimensionless, whereas AUCH is expressed in minutes and represents the cumulative wettability response over the complete evaporation process. For each sessile water drop, the integration endpoint corresponds to its own final measurable evaporation time, T.

For the experimental data obtained at the equal 5 min intervals, the integral was evaluated using the trapezoidal rule:

$$AUC_H \approx \sum_{i=1}^{N-1} \frac{H_I + H_{i+1}}{2}\Delta t \tag{8}$$

where H_i and H_{i+1} are the consecutive values of the normalized wettability parameter and times t_i and t_{i+1}, respectively, and Δt = 5 min in the constant intervals between consecutive measurements.

The conventional contact-angle AUC, expressed in °·min, represents the time-integrated apparent contact angle over the complete evaporation process. Higher values reflect the combined contribution of larger apparent contact angles and/or a longer evaporation duration. They should not be interpreted alone as a direct measure of reduced wettability, because θ(t) is also affected by evaporation mode, contact-line pinning/depinning, substrate heterogeneity, sessile water drop volume, temperature, humidity, and solid–liquid interactions. In the Young–Laplace framework, the drop shape is governed by the balance between capillary pressure and surface-tension forces. Therefore, the time evolution of the apparent contact angle reflects changes in interfacial curvature and capillary equilibrium during evaporation. The AUC parameter integrates these time-dependent geometrical and interfacial changes into a single quantitative descriptor of drop-geometry retention.

3.6. Goniometrical Results of Mylar 1 and Mylar 2 Samples. Comparative Analysis with AUC Integrals

Representative goniometric images of the sessile drops on Mylar 1 and Mylar 2 are shown in Figure 4.

The initial apparent contact angles differed between the two Mylar surfaces. Distilled water on untreated Mylar 1 exhibited an initial apparent contact angle of 67.2°, whereas on factory corona-treated Mylar 2, the initial apparent contact angle was 61.1°. The lower initial contact angle on Mylar 2 indicates greater wettability of the corona-treated surface. The measurements were performed at 5 min intervals. Because the same distilled water was used on both surfaces, the observed differences in θ(t), the full-process AUC, H(t), and evaporation duration are primarily attributed to the different surface states of

Mylar 1 and Mylar 2. This interpretation is consistent with the XPS results, indicating a higher surface O/C atomic ratio, consistent with possible differences in surface oxidation, for factory corona-treated Mylar 2. AUC provides a time-integrated measure of the apparent contact-angle response, whereas H(t) expresses the same measurements as a dimensionless apparent wettability parameter. Possible relationships between evaporation dynamics and interfacial hydrogen-bond organization remain hypothetical and cannot be established from contact-angle measurements alone [9].

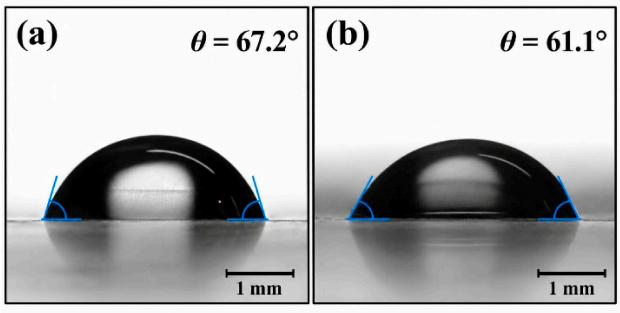


Figure 4. Representative goniometric images of sessile distilled-water drops on Mylar 1 (**a**) and Mylar 2 (**b**) at the initial measurement stage, illustrating the difference in apparent contact angle between the untreated and factory corona-treated BoPET surfaces.

3.7. Instantaneous Contact-Angle Retention Parameter

In the present study, the temporal evolution of the apparent contact angle, θ(t), obtained via the geometrical–optical method [9], is further used to derive dimensionless parameters characterizing the contact-angle retention and evaporation-related interfacial relaxation. A normalized parameter, denoted as the contact-angle retention parameter $I_{(\theta)}$, is defined as:

$$I_{(\theta)}(t) = \frac{\theta(t)}{\theta_0} \tag{9}$$

where θ_0 is the initial contact angle at t = 0.

This parameter represents the relative preservation of the apparent contact-angle state over time. Since the apparent contact angle reflects the balance between surface tension, adhesion, contact-line behavior, evaporation mode, and droplet geometry, the decrease in θ(t) during evaporation should be interpreted primarily as evaporation-related geometrical relaxation. It may be consistent with differences in interfacial molecular organization, but it is not a direct measure of structural cooperativity within the hydrogen-bond network.

Integral Contact-Angle Retention Parameter

To account for both the magnitude and duration of apparent contact-angle retention over the complete evaporation process, an integral parameter is introduced:

$$AUC = \int_{t_0}^{T} \theta(t)dt \tag{10}$$

For discrete experimental data, this integral is evaluated numerically using the trapezoidal rule:

$$I_{(\theta)int} = \sum_{i=1}^{n-1} \frac{I_{\theta,i} + I_{\theta,i+1}}{2} \Delta t \tag{11}$$

This parameter represents the time-integrated stability of the apparent contact-angle state, incorporating both:

- The persistence of larger contact angles,
- The duration of the complete evaporation process.

The integral contact-angle retention parameter is related to the area under the contact-angle curve:

$$I^*_{\theta,int} = \frac{AUC}{T\theta_0} \tag{12}$$

This relationship shows that $I^*_{\theta,int}$ represents the time-averaged normalized contact-angle retention over the complete evaporation process. Larger AUC values indicate a greater time-integrated apparent contact angle over the complete evaporation process, whereas $I^*_{\theta,int}$ describes the corresponding normalized time-averaged retention of the apparent contact angle.

Therefore, the proposed contact-angle-based indices provide a practical and non-invasive approach for evaluating relative differences in evaporation-related interfacial water organization between the control and investigated samples. However, these parameters should be interpreted as indirect macroscopic descriptors rather than as direct molecular measurements of hydrogen-bond number, hydrogen-bond energy, or hydrogen-bond lifetime.

The introduction of $I_{\theta(t)}$ and $I^*_{\theta,int}$ extends the geometrical–optical method by providing quantitative descriptors of the dynamic retention of the apparent contact angle during evaporation. This enables a deeper interpretation of sessile water drop evaporation behavior in terms of interfacial relaxation and possible differences in hydrogen-bond-related water organization.

The theoretical model of Luzar, Svetina, and Žekš related the surface free energy of water to hydrogen bonding in the interfacial layer [38]. Surface tension was not independently measured in the present study and is, therefore, not treated as an experimentally determinate variable.

3.8. Time-Dependent Normalized Wettability Parameter, H(t)

According to the Young–Dupré relation, the thermodynamic work of adhesion between a liquid and a solid surface is expressed as

$$W_A = \gamma LV(1 + cos) \tag{13}$$

where this represents the liquid–vapor surface tension and the equilibrium contact angle [39–42]. The work of cohesion of the liquid is [40,42]

$$W_C = 2\gamma LV \tag{14}$$

Therefore, the dimensionless ratio between adhesion and cohesion can be written as:

$$\frac{W_A}{W_C} = \frac{1 + cos}{2} \tag{15}$$

Equation (15) is valid for the equilibrium contact angle, whereas in the present study, H(t) is used as a descriptive parameter of apparent wettability during evaporation.

In the present study, the mathematical form of this relationship was used to define the dimensionless normalized wettability parameter H(t), as given in Equation (6). Higher H(t) values correspond to smaller apparent contact angles and greater apparent wettability.

Thus, H(t) is treated as a dimensionless apparent wettability parameter derived from the measured contact angle, rather than as a thermodynamic adhesion-to-cohesion work ratio. Higher H(t) values indicate lower apparent contact angles and greater apparent wettability [39–42]. In the present work, the extension of this relationship to the complete evaporation process provides a time-dependent description of wettability rather than a single static contact-angle value.

The measured apparent contact-angle values, θ(t), were transformed into the dimensionless normalized wettability parameter H(t) using the equation above. Because H(t)

increases as the apparent contact angle decreases, higher H(t) values correspond to greater wettability and lower contact angles during evaporation. Figure 5 shows the time evolution of H(t) for untreated Mylar 1 and factory corona-treated Mylar 2.

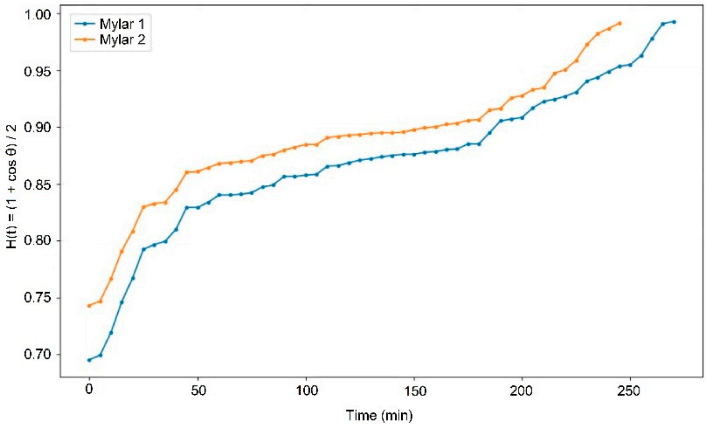


Figure 5. Time-dependent normalized wettability parameter, H(t), for distilled water on untreated Mylar 1 and factory corona-treated Mylar 2 during evaporation. H(t) was calculated from the measured apparent contact angle according to Formula (6). Higher H(t) values correspond to greater wettability.

At the initial measurement point, the apparent contact angle was 67.2° on Mylar 1 and 61.1° on Mylar 2, corresponding to H(0) values of 0.694 and 0.742, respectively. Thus, the factory corona-treated Mylar 2 exhibited an approximately 6.9% higher initial normalized wettability parameter than untreated Mylar 1. Throughout the common observation interval, H(t) remained generally higher for Mylar 2, consistent with its lower apparent contact-angle values and greater wettability. The difference became more pronounced during the later stages of evaporation, when the apparent contact angle on Mylar 2 decreased more rapidly.

Figure 5 demonstrates that factory corona-treated Mylar 2 exhibits consistently higher H(t) values and lower apparent contact angles than untreated Mylar 1, indicating greater apparent wettability under the same experimental conditions. The increase in H(t) during evaporation reflects the decrease in the apparent contact angle and does not, by itself, imply a change in the intrinsic surface properties of either Mylar film.

The higher H(t) values observed for factory corona-treated Mylar 2 are consistent with the XPS results, which showed an increased O/C atomic ratio and a greater contribution of oxygen-containing C–O and O–C=O surface functionalities. Taken together, the XPS and wettability results support the interpretation that increased surface oxidation is associated with a reduced apparent contact angle and enhanced wettability of the corona-treated BoPET surface.

3.9. Temporal Differences in Apparent Wettability Between Mylar 1 and Mylar 2

To visualize the temporal differences in apparent wettability between the two Mylar surfaces, $\Delta H(t) = H_{Mylar2}(t) - H_{Mylar1}(t)$ was evaluated at 50 corresponding time points over the common observation interval of 0–245 min, with measurements taken at 5 min intervals (Figure 6).

ΔH(t) values at all 50 corresponding time points were measured at 5 min intervals over the common observation period of 0–245 min. The positive values indicate greater apparent wettability of Mylar 2. The 50 time points were derived from the group-mean apparent contact angles of five independent sessile water drops (n = 5) for each Mylar surface, rather than from measurements of a single sessile drop.

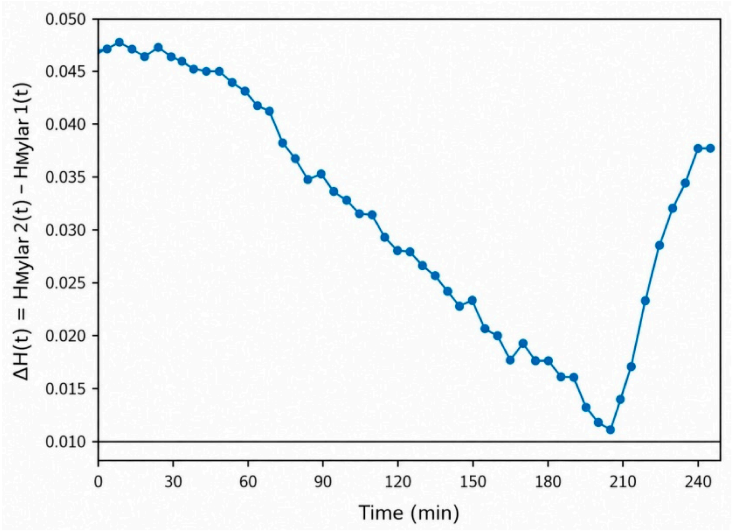


Figure 6. Time-dependent difference in the normalized apparent wettability parameter, $\Delta H(t) = H_{Mylar2}(t) - H_{Mylar1}(t)$, between untreated Mylar 1 and factory corona-treated Mylar 2 over the common observation interval of 0–245 min.

4. Conclusions

The optical-ring method and full-process AUC analysis revealed distinct evaporation-related wetting behavior of distilled water on untreated Mylar 1 and factory corona-treated Mylar 2. The complete evaporation process yielded AUC values of 11,023.06 ± 60.06 °·min over 270 min for Mylar 1 and 9322.70 ± 26.10 °·min over 245 min for Mylar 2. These full-process integrals incorporate both the magnitude of the apparent contact angle and the duration of evaporation. However, the limited availability of the original XPS spectra restricts verification of the proposed surface-chemical interpretation.

XPS showed an increase in the O/C atomic ratio from approximately 0.32 to 0.47 for Mylar 2, together with increased oxygen-containing surface functionalities.

Mylar 2 exhibited a lower initial apparent contact angle (61.1° vs. 67.2°) and higher $H(0)$ value (0.742 vs. 0.694). $H(t)$ is interpreted as a dimensional apparent wettability parameter. The results indicate that full-process integral analysis provides information on dynamic wettability that cannot be represented by a single initial contact-angle value alone.

The methodological contribution is the combined application of the previously validated optical-ring method, drop-by-drop AUC analysis over a common interval, and $H(t)$ to compare two BoPET surface states. Building on earlier studies of evaporation-driven contact-angle evolution, this approach provides a reproducible numerical summary of the measured trajectories alongside their time-resolved representation. Its added value is an integrated comparison of apparent wetting behavior; it does not establish a new molecular mechanism or directly measure changes in the hydrogen-bond network.

Author Contributions: Conceptualization, I.I. and Y.G.M.; methodology, I.I. and Y.G.M.; software, G.G.; validation, I.I. and Y.G.M.; formal analysis, P.V. and G.G.; investigation, I.I., A.I.I. and Y.G.M.; resources, P.V. and I.I.; data curation, P.V., A.I.I. and I.I.; writing—original draft preparation, I.I., Y.G.M., G.G. and P.V.; writing—review and editing, P.V. and A.I.I.; visualization, I.I., A.I.I. and G.G.; supervision, G.G.; project administration, I.I. and Y.G.M.; funding acquisition, Y.G.M. and I.I. All authors have read and agreed to the published version of the manuscript.

Funding: This research was funded by the Bulgarian National Science Fund, grant number KP-06-N68/3.

Data Availability Statement: The original contributions presented in this study are included in the article. Further inquiries can be directed to the corresponding author.

Conflicts of Interest: The authors declare no conflicts of interest.

References

1. Antonov, D.V.; Islamova, A.G.; Strizhak, P.A. Hydrophilic and hydrophobic surfaces: Features of interaction with liquid drops. *Materials* **2023**, *16*, 5932. [CrossRef] [PubMed]
2. Roosta, A.; Zendehboudi, S.; Rezaei, N. Estimating advancing and receding contact angles for pure and mixed liquids on smooth solid surfaces using the PCP-SAFT equation of state. *Phys. Chem. Chem. Phys.* **2025**, *27*, 6031–6042. [CrossRef] [PubMed]
3. Wilson, S.K.; D'Ambrosio, H.-M. Evaporation of sessile droplets. *Annu. Rev. Fluid Mech.* **2023**, *55*, 481–509. [CrossRef]
4. Shamim, J.A.; Takahashi, Y.; Goswami, A.; Shaukat, N.; Hsu, W.-L.; Choi, J.; Daiguji, H. Suppression of wetting transition on evaporative fakir droplets by using slippery superhydrophobic surfaces with low depinning force. *Sci. Rep.* **2023**, *13*, 2368. [CrossRef] [PubMed]
5. Raynard, A.; Abbas, A.; Armstrong, S.; Wells, G.G.; McHale, G.; Sefiane, K.; Orejon, D. Tuning contact line dynamics on slippery silicone oil grafted surfaces for sessile droplet evaporation. *Sci. Rep.* **2024**, *14*, 1750. [CrossRef] [PubMed]
6. de Gennes, P.G. Wetting: Statics and dynamics. *Rev. Mod. Phys.* **1985**, *57*, 827. [CrossRef]
7. Good, R.J. Contact angle, wetting, and adhesion: A critical review. *J. Adhes. Sci. Technol.* **1992**, *6*, 1269–1302. [CrossRef]
8. Kavuri, S.; Sharma, C.S.; Karapetsas, G.; Sahu, K.C. Evaporation of sessile drops on a heated superhydrophobic substrate. *Langmuir* **2025**, *41*, 23003–23014. [CrossRef] [PubMed]
9. Ignatov, I.; Marinov, Y.G.; Todorov, D.; Gluhchev, G.; Vassileva, P.; Ivanov, G.R.; Iliev, M.T. Geometrical-optical determination of the apparent contact angle of sessile water drops: A multiscale perspective on hydrogen-bond cooperativity. *Water* **2026**, *18*, 900. [CrossRef]
10. Bourges-Monnier, C.; Shanahan, M.E.R. Influence of evaporation on contact angle. *Langmuir* **1995**, *11*, 2820–2829. [CrossRef]
11. Hu, H.; Larson, R.G. Evaporation of a sessile droplet on a substrate. *J. Phys. Chem. B* **2002**, *106*, 1334–1344. [CrossRef]
12. Gelderblom, H.; Diddens, C.; Marin, A. Evaporation-driven liquid flow in sessile droplets. *Soft Matter* **2022**, *18*, 8535–8553. [CrossRef] [PubMed]
13. Picknett, R.G.; Bexon, R. The evaporation of sessile or pendant drops in still air. *J. Colloid Interface Sci.* **1977**, *61*, 336–350. [CrossRef]
14. Nurmi, H.A.; Zenuni, G.; Lepikko, S.; Saine, R.; Vuckovac, M.; Ras, R.H.A. In situ error analysis in contact angle goniometry. *Soft Matter* **2025**, *21*, 2422–2429. [CrossRef] [PubMed]
15. Campbell, J.M.; Christenson, H.K. Dynamic Measurement of low contact angles by optical microscopy. *ACS Appl. Mater. Interfaces* **2018**, *10*, 16893–16900. [CrossRef] [PubMed]
16. Rowan, S.M.; Newton, M.I.; McHale, G. Evaporation of microdroplets and the wetting of solid surfaces. *J. Phys. Chem.* **1995**, *99*, 13268–13271. [CrossRef]
17. Erbil, H.Y.; McHale, G.; Rowan, S.M.; Newton, M.I. Determination of the receding contact angle of sessile drops on polymer surfaces by evaporation. *Langmuir* **1999**, *15*, 7378–7385. [CrossRef]
18. Orejon, D.; Sefiane, K.; Shanahan, M.E.R. Stick–slip of evaporating droplets: Substrate hydrophobicity and nanoparticle concentration. *Langmuir* **2011**, *27*, 12834–12843. [CrossRef] [PubMed]
19. Stauber, J.M.; Wilson, S.K.; Duffy, B.R.; Sefiane, K. Evaporation of droplets on strongly hydrophobic substrates. *Langmuir* **2015**, *31*, 3653–3660. [CrossRef] [PubMed]
20. Starinskaya, E.; Miskiv, N.; Terekhov, V.; Safonov, A.; Li, Y.; Lei, M.-K.; Starinskiy, S. Evaporation dynamics of sessile and suspended almost-spherical droplets from a biphilic surface. *Water* **2023**, *15*, 273. [CrossRef]
21. Tian, W.; Wu, K.; Chen, Z.; Lei, Z.; Gao, Y.; Chen, Z.; Liu, Y.; Hou, Y.; Zhu, Q.; Li, J. Dynamic wetting of solid-liquid-liquid system by molecular kinetic theory. *J. Colloid Interface Sci.* **2020**, *579*, 470–478. [CrossRef] [PubMed]
22. Srinivasan, S.; McKinley, G.H.; Cohen, R.E. Assessing the accuracy of contact angle measurements for sessile drops on liquid-repellent surfaces. *Langmuir* **2011**, *27*, 13582–13589. [CrossRef] [PubMed]
23. Antonov, D.V.; Starinskaya, E.M.; Starinskiy, S.V.; Miskiv, N.B.; Terekhov, V.V.; Strizhak, P.A.; Sazhin, S.S. Heating and evaporation of sessile droplets: Simple and advanced models. *Langmuir* **2024**, *40*, 2656–2663. [CrossRef] [PubMed]
24. Barbaro, G.; Galdi, M.R.; Di Maio, L.; Incarnato, L. Effect of BOPET Film Surface Treatments on Adhesion Performance of Biodegradable Coatings for Packaging Applications. *Eur. Polym. J.* **2015**, *68*, 80–89. [CrossRef]
25. Ding, L.; Shao, L.; Bai, Y. Deciphering the Mechanism of Corona Discharge Treatment of BOPET Film. *RSC Adv.* **2014**, *4*, 21782–21787. [CrossRef]
26. Strobel, M.; Lyons, C.S.; Strobel, J.M.; Kapaun, R.S. Analysis of Air-Corona-Treated Polypropylene and Poly(ethylene terephthalate) Films by Contact-Angle Measurements and X-ray Photoelectron Spectroscopy. *J. Adhes. Sci. Technol.* **1992**, *6*, 429–443. [CrossRef]
27. DuPont Teijin Films. Mylar® LB: Product Information. Available online: https://www.tekra.com/sites/default/files/pet/Mylar_LB.pdf (accessed on 22 October 2026).

28. Slavov, D.; Tomaszewska, E.; Grobelny, J.; Drenchev, N.; Karashanova, D.; Peshev, Z.; Bliznakova, I. FTIR spectroscopy revealed nonplanar conformers, chain order, and packaging density in diOctadecylamine- and octadecylamine-passivated gold nanoparticles. *J. Mol. Struct.* **2024**, *1314*, 138827. [CrossRef]
29. Ignatov, I.; Marinov, Y.G.; Vassileva, P.; Popova, T.P.; Gluhchev, G.; Iliev, M.T.; Huether, F.; Dimitrov, Z.; Gotova, I. Formation of ice Ih clusters in solid-phase glacial water with low concentrations of Ca^{2+} and Mg^{2+} ions. *Crystals* **2025**, *15*, 254. [CrossRef]
30. Ignatov, I.; Marinov, Y.G.; Vassileva, P.; Gluhchev, G.; Pesotskaya, L.A.; Jordanov, I.P.; Iliev, M.T. Nonlinear hydrogen bond network in small water clusters: Combining NMR, DFT, FT-IR, and EIS research. *Symmetry* **2025**, *17*, 1062. [CrossRef]
31. Amirov, I.I.; Alov, N.V.; Sharanov, P.Y.; Rakhimova, T.V. Oxidation and etching of thin ruthenium films in low ion energy oxygen plasma. *J. Surf. Investig.* **2024**, *18*, 1359–1363. [CrossRef]
32. Ghobeira, R.; EsbahTabaei, P.S.; Morent, R.; De Geyter, N. Chemical Characterization of Plasma-Activated Polymeric Surfaces via XPS Analyses: A Review. *Surf. Interfaces* **2022**, *31*, 102087. [CrossRef]
33. Ignatov, I.; Drossinakis, C.; Ignatov, A.I. Color Coronal Spectral Analysis: Results with Water Solution of Calcium Carbonate. *Port. Electrochim. Acta* **2025**, *43*, 113–126. [CrossRef]
34. Ignatov, I.; Pesotskaya, L.; Glukhova, N.; Yevdokymenko, N.; Popova, T.P.; Ignatov, A.I.; Stoyanov, C. Registration of different types of water with corona gas discharge effects and parameters of brightness. *Port. Electrochim. Acta* **2025**, *43*, 219–226. [CrossRef]
35. Ignatov, I.; Pesotskaya, L.; Glukhova, N.; Popova, T.P.; Mladenova, A.; Bankova, R.; Ignatov, A.I. Results of experimental studies on electric corona gas discharge of Bulgarian lavender oil. *Port. Electrochim. Acta* **2026**, *44*, 303–312. [CrossRef]
36. Matthews, J.N.S.; Altman, D.G.; Campbell, M.J.; Royston, P. Analysis of serial measurements in medical research. *Br. Med. J.* **1990**, *300*, 230–235. [CrossRef] [PubMed]
37. Fekedulegn, D.B.; Andrew, M.E.; Burchfiel, C.M.; Violanti, J.M.; Hartley, T.A.; Charles, L.E.; Miller, D.B. Area under the curve and other summary indicators of repeated waking cortisol measurements. *Psychosom. Med.* **2007**, *69*, 651–659. [CrossRef] [PubMed]
38. Luzar, A.; Svetina, S.; Žekš, B. The contribution of hydrogen bonds to the surface tension of water. *Chem. Phys. Lett.* **1983**, *96*, 485–490. [CrossRef]
39. Gutowski, W. Physico-chemical criteria for maximum adhesion. Part I: Theoretical concepts and experimental evidence. *J. Adhes.* **1985**, *19*, 29–49. [CrossRef]
40. Pogorzelski, S.; Janowicz, P.; Dorywalski, K.; Boniewicz-Szmyt, K.; Rochowski, P. Wettability, adsorption and adhesion in polymer (PMMA)—Commercially available mouthrinse system. *Materials* **2023**, *16*, 5753. [CrossRef] [PubMed]
41. Pawlak, Z.; Petelska, A.D.; Urbaniak, W.; Yusuf, K.Q.; Oloyede, A. Relationship between wettability and lubrication characteristics of the surfaces of contacting phospholipid-based membranes. *Cell Biochem. Biophys.* **2013**, *65*, 335–345. [CrossRef] [PubMed]
42. Ha, J.-H.; Kim, H.-C.; Kim, Y.K.; Kwon, T.-Y. An evaluation of wetting and adhesion of three bioceramic root canal sealers to intraradicular human dentin. *Materials* **2018**, *11*, 1286. [CrossRef] [PubMed]

Disclaimer/Publisher's Note: The statements, opinions and data contained in all publications are solely those of the individual author(s) and contributor(s) and not of MDPI and/or the editor(s). MDPI and/or the editor(s) disclaim responsibility for any injury to people or property resulting from any ideas, methods, instructions or products referred to in the content.